Broadband green to broadband deep red modulation of Bi^{3+} luminescence in Lu_2WO_6 by Gd^{3+} doping and application in high color rendering index white LED and Near-infrared LED

Xuejiao Wang,[a,b*] Xiaowen Feng,[a] Maxim S. Molokeev,[c,d,e] Huiling Zheng,[a] Qiushi Wang,[a] Chunyan Xu,[f] Ji-Guang Li[b*]

[a]College of Chemistry and Materials Engineering, Bohai University, Jinzhou, Liaoning 121007, China

[b]Research Center for Functional Materials, National Institute for Materials Science, Tsukuba, Ibaraki 305-0044, Japan

[c]Laboratory of Crystal Physics, Kirensky Institute of Physics, FRC KSC SB RAS, Krasnoyarsk 660036, Russia

[d]Research and Development Department, Kemerovo State University, Kemerovo 650000, Russia

[e]Siberian Federal University, Krasnoyarsk 660041, Russia

[f]Jilin Engineering Laboratory for Quantum Information Technology, Institute for Interdisciplinary Quantum Information Technology, Jilin Engineering Normal University, Changchun 130052, China

*Corresponding author

Dr. Xuejiao Wang
Bohai University
Jianzhou, China
Tel: +86-416-3400708
E-mail: wangxuejiao@bhu.edu.cn

Dr. Ji-Guang Li
National Institute for Materials Science
Ibaraki, Japan
Tel: +81-29-860-4394
E-mail: li.jiguang@nims.go.jp

Abstract

Phosphors that exhibit tunable broadband emissions are highly desired in multi-functional LEDs, including pc-WLEDs and pc-NIR LEDs. In this work, broadband emissions were obtained and modulated in the unexpectedly wide spectral range of 517-609 nm for $(Lu_{0.99-x}Gd_xBi_{0.01})_2WO_6$ phosphors *via* tuning the Gd^{3+} content (x = 0-0.99). The effects of Gd^{3+} doping on phase constituent, particle morphology, crystal structure, and photoluminescence were systematically investigated. Broadband green emission was obtained with the Gd^{3+}-free $(Lu_{0.99}Bi_{0.01})_2WO_6$ phosphor (x = 0), whose emission intensity was enhanced by 50% with 5 at% of Gd^{3+} (x = 0.05). Phase transition happened when $x > 0.50$, and broadband red-NIR emission was obtained when x = 0.75-0.99. Three luminescence centers were proved to be responsible for the broadband emissions *via* crystal structure, spectral fitting and fluorescence decay analysis. A pc-WLED with high color rendering index (Ra = 91.3), stable emission color, and low color temperature (3951 K) was fabricated from the $(Lu_{0.94}Gd_{0.05}Bi_{0.01})_2WO_6$ broadband green phosphor, and an LED device that simultaneously emits high color rendering white light and NIR light was obtained with the $(Gd_{0.99}Bi_{0.01})_2WO_6$ broadband red-NIR phosphor. Night version and noninvasive imaging were also demonstrated for the latter LED device.

***Keywords*:** Broadband Bi^{3+} luminescence, Gd^{3+} doping, Rare earth tungstate

1. Introduction

Phosphors-converted LEDs (pc-LEDs), either traditional white light pc-WLEDs or recently on the rise near-infrared (NIR) pc-LEDs, have various advantages and are finding wide applications in the fields of general lighting, night vision, non-destructive analysis, biomedical, and so forth.[1-4] Phosphors play a decisive role in pc-LEDs and determine the quality of the devices. For the fabrication of pc-WLEDs, one typical route is to combine red-green-blue (RGB) emitting phosphors with a UV LED chip or to pump a blend of red and green phosphors by a blue LED chip.[5,6] However, due to the lack of a cyan (470-510 nm) spectral component between the PL spectra of blue and green phosphors, the obtained pc-WLEDs have a low color rendering index (CRI, 70-80), which limits their wide applications in general lighting.[7,8] To address the cyan gap, developing UV or blue light excitable cyan-emitting phosphors becomes a logical-led solution, and thus considerable attention was paid to the synthesis of cyan emitting phosphors to enhance the CRI of the pc-LED devices.[7,9-13] Though the CRI of a pc-LED device incorporating a cyan phosphor can indeed be improved in this way, the use of multiple phosphors will lead to fabrication complexity and reabsorption. Therefore, phosphors that emit broadband green light covering the cyan gap have been developed and used for high CRI and low correlated color temperature (CCT) pc-WLED devices.[14,15] However, the development of such phosphors is yet rather limited, and the current research is mainly focused on garnet hosts with Eu^{2+} and Ce^{3+} as activators.[14,15]

Another route to obtain pc-WLED is coating a blue LED chip with the yellow-emitting $Y_3Al_5O_{12}:Ce^{3+}$ phosphor ($YAG:Ce^{3+}$) but has the shortcoming of low CRI (<75) and unwanted high CCT (~7750 K, cold white) due to the lack of red spectral components. For this, various red phosphors have been developed and

applied for white lighting. In the meantime, NIR phosphors are under keen development for NIR-pc LED applications.[1-4] Red light is adjacent to NIR light in the electromagnetic spectrum, and broadband-emitting red phosphors may thus cover the NIR region for simultaneous white and NIR light applications. Therefore, broadband green and broadband red phosphors are both highly desired.

Bismuth is an intriguing element in that it has various valance states (Bi^0, Bi^{1+}, Bi^{2+}, Bi^{3+}, Bi^{5+}).[5,16-18] Amongst, Bi^{3+} ([Xe] $4f^{14}5d^{10}6s^2$ configuration) is relatively stable and easy to get valence. The 6*s* electrons of Bi^{3+} are susceptive to the surrounding environment, for which the emission position and excitation tail of Bi^{3+}-doped phosphors are strongly dependent on crystal field and lattice covalency.[19-22] Hence, by adjusting the host composition and crystal structure, tunable Bi^{3+} luminescence can be achieved. In this work, Bi^{3+} doped Lu_2WO_6 tungstate was synthesized *via* solid state reaction, and the luminescence of Bi^{3+} was successfully tuned from broadband green to broadband red-NIR *via* Gd^{3+} doping. High color rendering LED devices for general lighting and NIR lighting were also obtained with such phosphors.

2. Experimental section

2.1. Reagents and synthesis.

The series of $(Lu_{0.99-x}Gd_xBi_{0.01})_2WO_6$ (x = 0-0.99) phosphors were synthesized *via* solid-state reaction, which was started with Lu_2O_3 (99.99% pure), Gd_2O_3 (99.99% pure), Bi_2O_3 (99.99% pure) and $H_{40}N_{10}O_{41}W_{12}$ xH_2O (AR grade). All the reagents were bought from Aladdin Industrial Corporation (Shanghai, China). The starting materials were weighed according to the above formula, and the amount of $H_{40}N_{10}O_{41}W_{12}$ xH_2O was 6 wt% in excess in each case to compensate evaporation

loss. The mixture was thoroughly ground in an agate mortar for 30 min and subsequently calcined in a muffle furnace at 1300 ^{o}C for 4 h with a heating rate of 5 ^{o}C/min at the ramp stage. The products were cooled to room temperature at 5 ^{o}C/min and were then slightly grounded for characterizations.

2.2. Fabrication of LED devices.

Two LED devices were fabricated using the broadband green and broadband red-NIR phosphors obtained in this work. The LED1 for full-spectrum pc-WLED was fabricated by thoroughly mixing commercial $CaAlSiN_3:Eu^{2+}$ red phosphor (main emission at 640-650 nm; Intematix Co., Ltd, California, USA), commercial $BaMgAl_{10}O_{17}:Eu^{2+}$ blue phosphor (BAM, main emission at 440-460 nm; Yantai Shield, Yantai, China) and the synthesized $(Lu_{0.94}Gd_{0.05}Bi_{0.01})_2WO_6$ broadband green phosphor in silicone (Leaftop 9300, Shengzhen Tegu New Materials Co., Ltd, Shenzhen, China), followed by coating on a 1 W NUV-LED chip (~365 nm emission; San'an Optoelectronics Co., Ltd, Xiamen, China), where the weight ratio of the above three phosphors is 4:1:2 and the weight ratio of total phosphor powder to silicone is 1:1. The LED2 for simultaneous white and NIR lighting was fabricated by blending the BAM phosphor and the prepared $(Gd_{0.99}Bi_{0.01})_2WO_6$ broadband red-NIR phosphor in silicone, followed by coating on another NUV-LED chip, where weight ratio of the two phosphors is 1:4 and the weight ratio of total phosphor to silicone is 1:1.

2.3. Characterization.

Phase identification was performed by X-ray diffractometry (XRD; Model Ultima IV, Rigaku, Tokyo, Japan) operated at 40 kV/40 mA, using nickel filtered Cu-K_α

radiation (λ=0.15406 nm) and a scanning speed of 2 °/min. Rietveld refinement was carried out using the TOPAS software.[23] The crystallographic data were deposited in Cambridge Crystallographic Data Centre (CSD#2213277-2213283), and can be downloaded from the website (www.ccdc.cam.ac.uk/data_request/cif). The morphology and elemental distribution of the samples were analyzed by field emission scanning electron microscopy (FE-SEM; Model Tescan MIRA LMS, Tesken, Czech Republic) equipped with an energy dispersive spectrometer (EDS). X-ray photoelectron spectroscopy (XPS) of the valence state of Bi was conducted using a Thermo Scientific K-Alpha analyzer (Thermo Fisher Scientific, Waltham, USA), where the chamber pressure is less than 2.0×10^{-7} Mbar, the spot size is 400 μm, the working voltage is 12 kV, and the filament current is 6 mA. The L_3-edge X-ray absorption spectrum of Bi was measured at the XRD station of beamline 4B9A of Beijing Synchrotron Radiation Facility (BSRF) in the fluorescence mode. Light absorption and bandgap energy were studied *via* UV-vis spectroscopy (Model PE-750, PerkinElmer, Waltham, USA). Photoluminescence was measured using an FLS 1000 fluorospectrophotometer (Edinburgh Instruments Ltd., Edinburgh, UK) with a 450 W Xe lamp for excitation, slit width of 1 nm for excitation and 0.7 nm for emission, a scanning speed of 1 nm/s, and a TAP-02 accessory for temperature control. The quantum yield and fluorescence decay were recorded using the integrating sphere system and the lifetime testing unit of the FLS 1000 equipment, respectively. The optical properties of the fabricated LEDs were measured by a Model OHSP-350M LED Fast-Scan Spectrophotometer (350-1050 nm range, Hangzhou Hopoo

Light&Color Technology Co. Ltd., Hangzhou, China). The density of states of two typical samples were calculated using the Vienna ab initio simulation package (VASP) with the projector augmented wave (PAW) potential, where the exchange–correlation potential was treated with the generalized gradient approximation using the Perdew–Burke–Ernzerhof (PBE) function.[24]

3. Results and discussion

3.1 Phase composition, crystallite morphology, and crystal structure

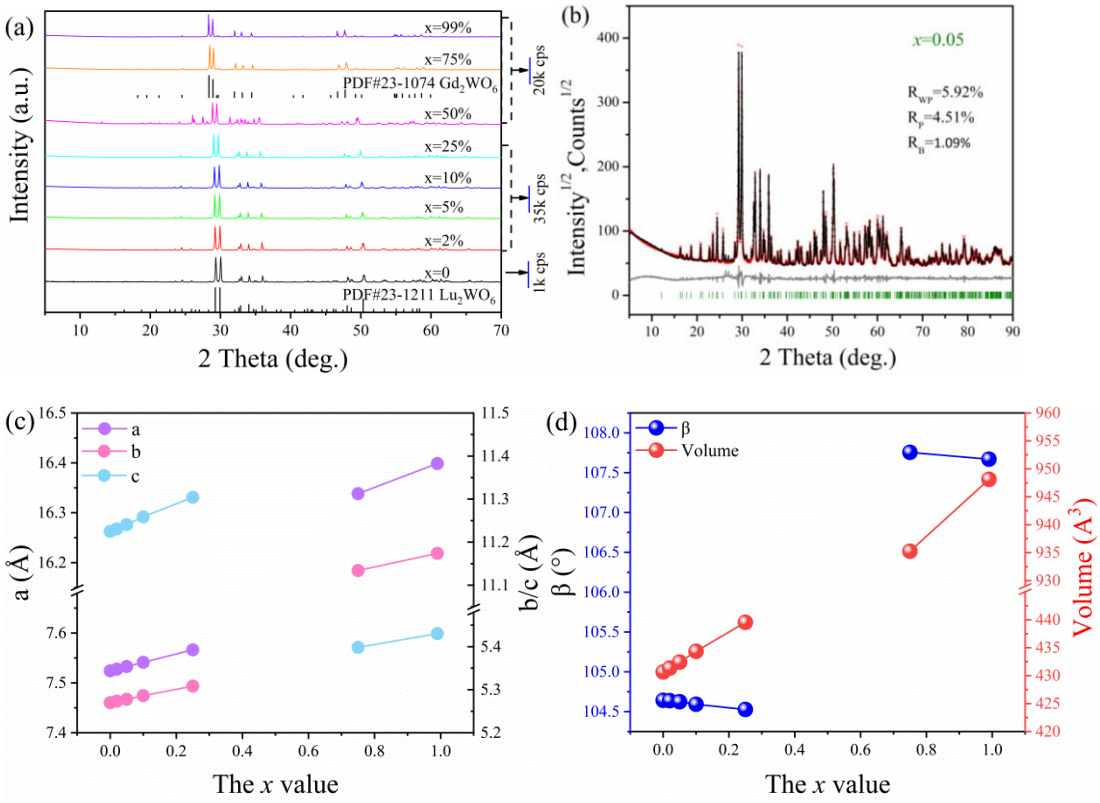

Fig. 1 The XRD patterns of $(Lu_{0.99-x}Gd_xBi_{0.01})_2WO_6$ (x = 0-0.99) (a), the observed (black) and calculated (red) XRD profiles and the difference (gray) between the two for the $(Lu_{0.94}Gd_{0.05}Bi_{0.01})_2WO_6$ sample (x = 0.05) (b), where the Bragg reflections are indicated with green tick marks, and the correlation of lattice constants (c) and axis angle/cell volume (d) with the x value.

Fig. 1a shows the XRD patterns of the products, it can be perceived from the diffraction intensity that Gd^{3+} doping greatly enhanced the crystallinity of the sample. Such a phenomenon is closely related to a gradual change in crystallite morphology

and will be explained later. The x = 0-0.25 samples can be well indexed to the monoclinic Lu_2WO_6 (PDF card No. 23-1211; $P2/c$ space group) due to the similar ionic radii of Lu^{3+} (0.977 Å for CN = 8) and Gd^{3+} (1.053 Å for CN = 8). A phase mixture was resulted at x = 0.50 and a complete phase transition to monoclinic Gd_2WO_6 (PDF card No. 23-1074; $C2/c$ space group) happened at x = 0.75. Starting from the crystal structures of Lu_2WO_6[25] and Gd_2WO_6[26], Rietveld refinement using the TOPAS 4.2 software[24] yielded stable results and satisfactory R-factors (Table S1) for the two series of compounds (Fig. S1), as shown in Fig. 1b with the x = 0.05 sample for example. The derived atomic coordinates and main bond lengths are summarized in Table S2 and Table S3, respectively. The derived lattice constants (a, b, c), cell volume and axis angle (β) are shown in Fig. 1c,d, where it is seen that, except for axis angle, the structural parameters all monotonously increase with increasing Gd^{3+} doping. This proves the formation of solid solution and suggests that the designated chemical compositions are close to the real ones.

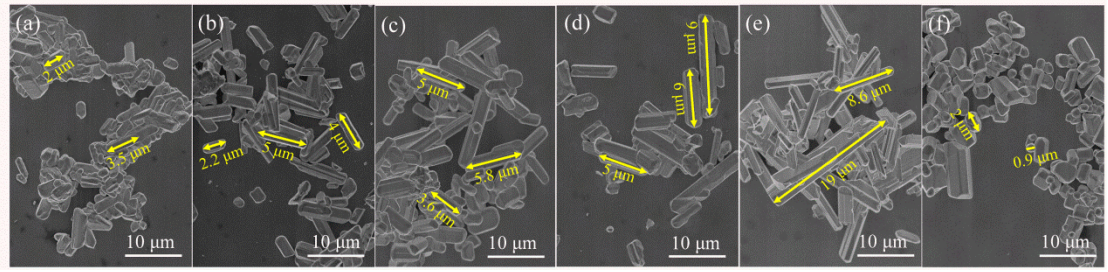

Fig. 2 FE-SEM morphologies of the $(Lu_{0.99-x}Gd_xBi_{0.01})_2WO_6$ samples with (a) x=0, (b) x=0.05, (c) x=0.10, (d) x=0.25, (e) x=0.50, and (f) x=0.99.

Product morphology was investigated *via* FE-SEM, and the results are shown in Fig. 2. It can be seen that, in most cases, irregular aggregates consisting of microrod-like crystallites were produced. The microrods grew longer with increasing Gd^{3+} doping until x = 0.50. This may be due to the fact that the formation of the $(Lu_{0.99-x}Gd_xBi_{0.01})_2WO_6$ final product is the reaction of RE_2O_3 (RE=Lu or Gd; Lewis

base) and $H_{40}N_{10}O_{41}W_{12}$ (Lewis acid) at high temperatures. The basicity of Gd_2O_3 is stronger than Lu_2O_3 and, therefore, the oxides (Lewis base) more readily react with $H_{40}N_{10}O_{41}W_{12}$ (Lewis acid) with increasing portion of Gd_2O_3 in the reactant mixture. The rodlike morphology mostly vanished for the x = 0.99 sample owing to the different crystal structures of Lu_2WO_6 and Gd_2WO_6. Elemental maps of two typical samples revealed good composition homogeneity, as shown in Fig. 3 and Fig. S2 for $(Gd_{0.99}Bi_{0.01})_2WO_6$ and $(Lu_{0.94}Gd_{0.05}Bi_{0.01})_2WO_6$, respectively.

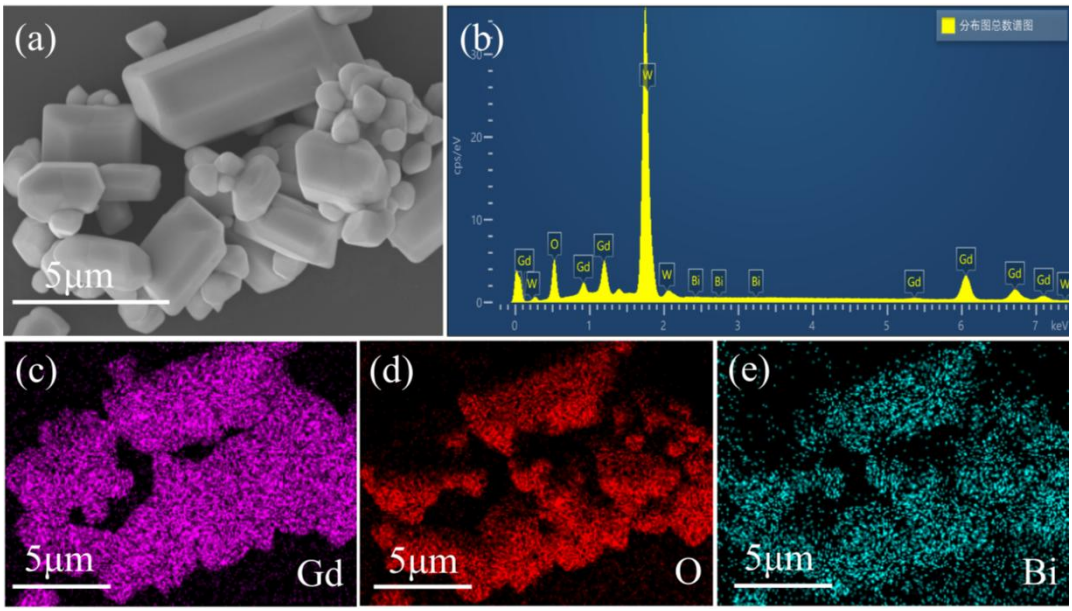

Fig. 3 SEM morphology (a), EDS analysis (b), and elemental mapping (c-e) of the $(Gd_{0.99}Bi_{0.01})_2WO_6$ sample.

As valence state strongly affects the luminescence of bismuth, it is necessary to make an analysis before further discussion. Fig. 4a shows the XPS survey spectra for the two typical samples of x = 0 and 0.99, from which it is obvious that all the spectral features, except for the C 1s level, are attributed to the constituent elements of $(Lu_{0.99-x}Gd_xBi_{0.01})_2WO_6$. Fig. 4b shows the high-resolution XPS spectra of Bi 4*f* orbital. It was observed that the peaks for Bi $^4f_{5/2}$ and Bi $^4f_{7/2}$ are located at around 164.31 and 159.01 eV with a doublet splitting of 5.30 eV for the x = 0 sample and at 163.65 and 158.43 eV with a doublet splitting of 5.22 eV for the x = 0.99 sample. This

is consistent with the Bi 4*f* spin-orbit and confirmed the existence of Bi^{3+} in the two samples.[27,28] The different splitting energy is due to change of the crystal structure. The observed doublet peaks for Bi $^4f_{7/2}$ and Bi $^4f_{5/2}$ are asymmetric in both the lattices, which is due to the fact that Bi^{3+} ions are located at multiple crystallographic sites, since the binding energy for Bi in different polyhedrons slightly varies. Furthermore, both the two peaks shifted to lower energy for the x = 0.99 sample, from 164.39 and 159.08 eV to 163.65 and 158.43 eV, respectively. This may be caused by a higher covalency of the Bi-O bond in $(Gd,Bi)_2WO_6$ than in $(Lu,Bi)_2WO_6$, since a higher covalency will cause a stronger nephelauxetic effect and make the electron easier to flee from the core.

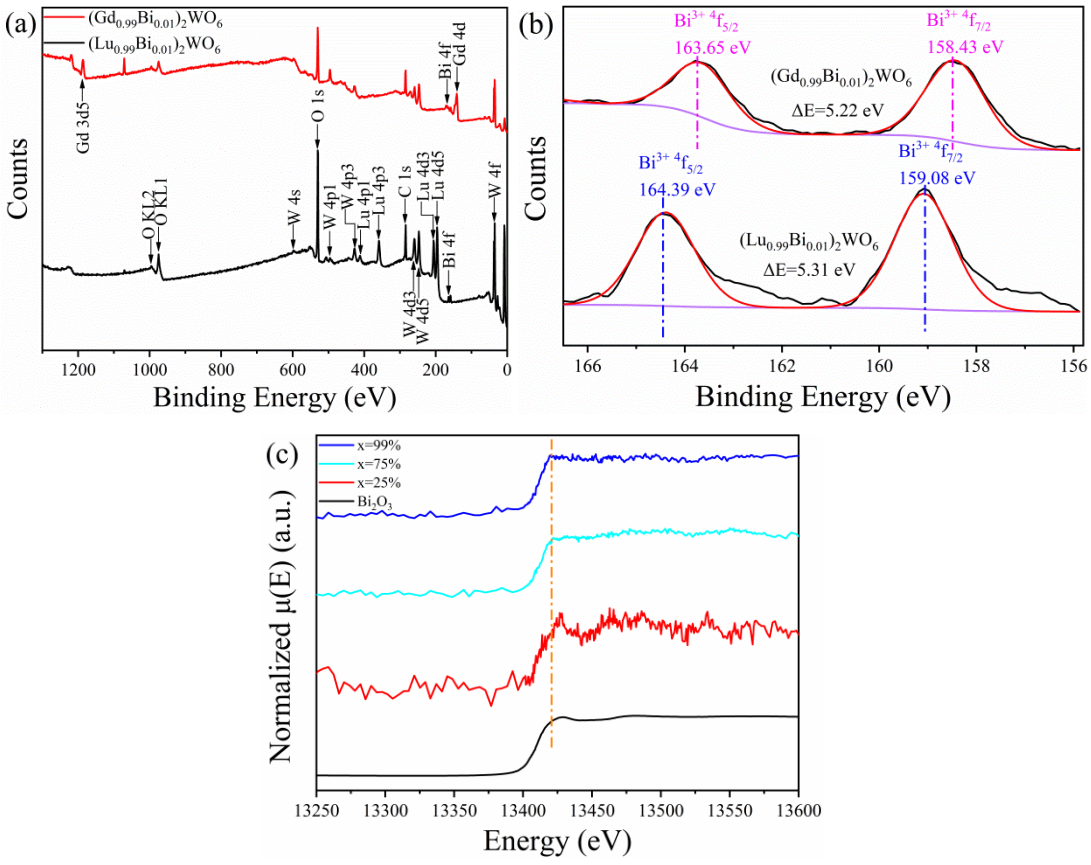

Fig. 4 XPS survey spectra (a) and high-resolution XPS spectra of Bi 4*f* orbital (b) for the x = 0 and 0.99 typical compositions. (c) is the Bi L_3-edge XANES spectra for the typical samples of x = 0.25, 0.75 and 0.99, with that of the Bi_2O_3 reference included for comparison.

Fig. 4c shows the results of X-ray absorption near edge structure (XANES) analysis of Bi L_3-edge for the three samples of x = 0.25, 0.75 and 0.99, using Bi_2O_3 as a

reference material. XANES is sensitive to the valence of absorption atoms and partly to the geometrical configuration of the surrounding atoms. The position of edge energy depends on the oxidation state of the absorption atoms, permitting the detection of the valence state of Bi.[29,30] It can be seen that the synthesized samples and Bi_2O_3 share the same position for the edge, which further proves that the valence state of Bi is 3+ in the studied samples.

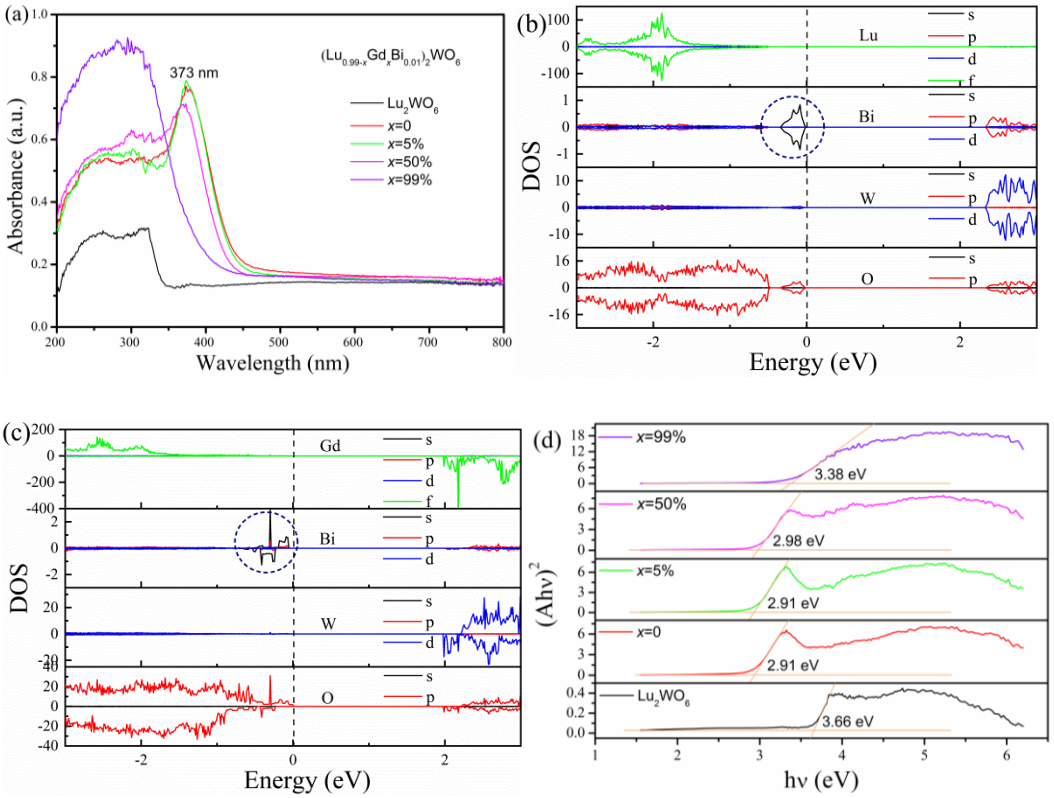

Fig. 5 UV-vis absorption spectra of $(Lu_{0.99-x}Gd_xBi_{0.01})_2WO_6$ (x = 0-0.99) (a), the partial density of states (DOS) of Bi, W, O, Gd/Lu atoms for $(Lu_{0.99}Bi_{0.01})_2WO_6$ (b) and $(Gd_{0.99}Bi_{0.01})_2WO_6$ (c), where the Fermi level is indicated by the vertical dashed line. Part (d) is for the determination of bandgap energies.

Fig. 5a shows the absorption spectra in the 200-800 nm region of typical samples, together with a Lu_2WO_6 powder synthesized in this work for comparison. It is seen that Lu_2WO_6 shows absorption in the 200-350 nm region, and 1 at% of Bi^{3+} doping of Lu_2WO_6 ($(Lu_{0.99}Bi_{0.01})_2WO_6$, x = 0) obviously enhanced the absorption and produced an intense new band at 373 nm that is contributed from $^1S_0 \rightarrow {}^3P_1$ transition of Bi^{3+}

orbitals.[31] Slight doping of Gd^{3+} (x = 0.05) did not obviously change the spectra. The x = 0.50 sample shows a similar spectral profile but lower intensity for the 373 nm band, and the 200-350 nm broadband is slightly stronger. When Lu^{3+} is completely replaced by Gd^{3+} (x = 0.99), the sample showed much stronger absorption in the 200-350 nm region and the 373 nm band disappeared. The absence of the 373 nm band was speculated to be due to the change of covalency experienced by Bi^{3+} and variation of electronic configuration for Bi^{3+} in the x = 0.99 sample. It was reported that the position of optical absorption for the $^1S_0 \rightarrow {}^3P_1$ transition of Bi^{3+} strongly depends on covalency effect/nephelauxetic strength in the crystal lattice.[32,33] Thus, it is reasonable to infer that the $^1S_0 \rightarrow {}^3P_1$ transition of Bi^{3+} would left-shift in the UV-vis spectrum and overlap with the broadband of tungstate anions (200-350 nm) when Lu^{3+} (electronegativity: 1.27 eV) is completely replaced by Gd^{3+} (electronegativity: 1.20 eV). In view that the variation of electronic configuration for Bi^{3+} may also influence UV absorption, the partial DOS of Bi, W, O, Gd/Lu atoms were calculated in Fig. 5b,c for the two typical compositions of x = 0 and 0.99. It can be seen that, for $(Lu_{0.99}Bi_{0.01})_2WO_6$ (x = 0), the valence band is mainly contributed from Lu 4*f* and O 2*p* and the conduction band is mainly composed of W 5*d* and O 2*p*, though Bi 6*s* and Bi 6*p* slightly contributed to the valence and conduction bands, respectively. For $(Gd_{0.99}Bi_{0.01})_2WO_6$ (x = 0.99), the valence band is composed of Gd 4*f*, O 2*p* and Bi 6*s* while the conduction band consists of Gd 4*f*, W 5*d* and O 2*p* states. The 6*s* states of Bi are near the Fermi surface in $(Lu_{0.99}Bi_{0.01})_2WO_6$ and obviously moves deeper into the valence band in $(Gd_{0.99}Bi_{0.01})_2WO_6$. Furthermore, the orbital hybridization of Bi and O is also more prominent in $(Gd_{0.99}Bi_{0.01})_2WO_6$. These suggest that the absorption of Bi^{3+} may overlap with that of tungstate anions and shift to a higher energy, which corresponds with the observed changing of absorption spectra. Estimation of bandgap

energy (E_g) can be made from the absorption spectra. The relation between absorption coefficient (α) and incident photon energy (hν) can be written as $\alpha=B_d(h\nu-E_g)^{1/2}$ for indirectly allowed transition.[34,35] The α in the equation represents absorption coefficient, B_d is absorption constant, and hν is the energy of incident photons. The $(Ah\nu)^2$-hν plots, converted from the spectral data of Fig. 5a, are shown in Fig. 5d, where *A* presents absorbance and is proportional to α. Extrapolating the linear parts of the $(Ah\nu)^2$-hν plots yielded E_g values of ~3.66, 2.91, 2.91 and 2.98 eV for Lu_2WO_6, $(Lu_{0.99}Bi_{0.01})_2WO_6$, $(Lu_{0.94}Gd_{0.05}Bi_{0.01})_2WO_6$ and $(Lu_{0.49}Gd_{0.50}Bi_{0.01})_2WO_6$, respectively. The $(Gd_{0.99}Bi_{0.01})_2WO_6$ sample, on the other hand, was found to have E_g value of 3.38 eV.

3.2 Photoluminescence properties

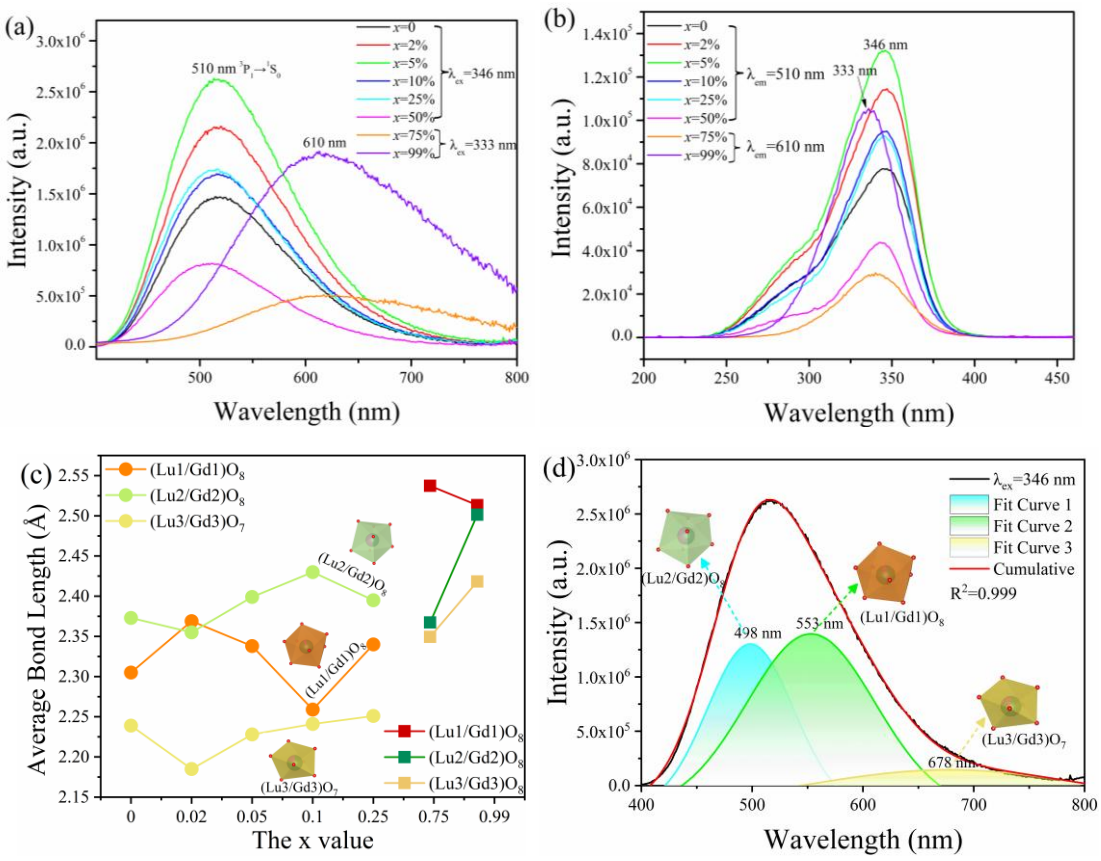

Fig. 6 The emission (a) and excitation (b) spectra of $(Lu_{0.99-x}Gd_xBi_{0.01})_2WO_6$ (x = 0-0.99), the average bond lengths (Å) of $(Lu_{1-x}Gd_x)O_n$ polyhedrons (c), and the results of Gaussian fitting of the emission spectrum of the x = 0.05 sample (d).

The effect of Gd^{3+} doping on Bi^{3+} luminescence was investigated, and Fig. 6a shows the emission spectra for the series of $(Lu_{0.99-x}Gd_xBi_{0.01})_2WO_6$ phosphors (x = 0-0.99; λ_{ex} = 346 nm). It is seen that the x = 0 sample exhibits a broad and asymmetric luminescence band ranging from 400 to 720 nm (peaking at 510 nm) that arises from the $^3P_1 \rightarrow {}^1S_0$ transition of Bi^{3+}. Noteworthy is that the band has a large full width at half maximum (FWHM) of 0.61 eV and well covers the cyan gap. Therefore, the phosphor may have the potential for application in high color rendering white pc-LEDs. When $x \leq 0.50$, Gd^{3+} doping did not obviously change the profile but influenced the intensity and position of Bi^{3+} luminescence. As seen from the relationship shown in Fig. S3, the 510 nm emission intensity increases until x = 0.05 and then decreases. The x = 0.10 and x = 0.25 samples have an almost equal intensity, which is still stronger than the Gd^{3+}-free sample (x = 0) although weaker than the x = 0.05 one. The increased luminescence with Gd^{3+} doping (x = 0.02 and 0.05) may largely be due to the enhanced crystallinity of the sample as analyzed in Fig. 2, while the decreased luminescence with further doping of Gd^{3+} (x = 0.10 and 0.25) may be due to lattice expansion (lower lattice stiffness), which enhances phonon vibration and strengthens phonon-photon coupling to some degree.[36-39] Besides, the intensified distortion of Bi-O polyhedron by Gd^{3+} doping is also harmful to the $^3P_1 \rightarrow {}^1S_0$ emission of Bi^{3+}, since the transition is parity allowed and can be suppressed by a larger extent of polyhedron distortion. The emission intensity of the x = 0.50 sample is even lower than the Gd^{3+}-free one, and this may be due to the multi-phase nature of this sample (Fig. 1). Furthermore, the normalized PL spectra revealed that the emission band tends to blue shift with increasing x for the x = 0-0.50 samples, as seen in Fig. S4.

The type of polyhedron and bond length are important factors determining the

crystal field strength (D_q) of the sites occupied by Bi^{3+} according to crystal field theory, and D_q can be estimated by the following expression:[40]

$$D_q = \frac{1}{6} Ze^2 \frac{r^4}{R^5} \qquad (1)$$

where *Z* is the charge of the ligand anion, *e* is the charge of electron, *r* is the radius of the *d* wave function, and *R* is the average distance between the central cation and its ligand anion. As D_q is inversely proportional to R^5, an increasing *R* would result in a smaller D_q. The average bond lengths of the three types of polyhedrons in the host were calculated according to the aforesaid results of Rietveld structure refinement, which are presented in Fig. 6c as a function of the Gd^{3+} content. It can therefore be concluded from the figure that the tending to be larger average bond length with increasing *x* is responsible for the observed blue shifting of emission band for the *x* = 0-0.25 samples.

The asymmetric profile of the broad green emission can be decomposed into three Gaussian sub-bands as shown in Fig. 6d for the *x* = 0.05 sample, which also indicates the presence of three kinds of luminescence centers. The results of Gaussian fitting for the other compositions can be found in Fig. S5 and Table S4. Basically, unchanged positions of the three sub-peaks were observed until *x* = 0.10, and a blue shift was observed with further doping at *x* = 0.25 and especially at *x* = 0.50. For the *x* = 0-0.25 $(Lu_{0.99-x}Gd_xBi_{0.01})_2WO_6$ samples, it was found from Fig. 6c that bond length decreases in the order (Lu,Gd)2–O > (Lu,Gd)1–O > (Lu,Gd)3–O and, therefore, the sub-peaks at ~500, 555 and 678 nm should arise from the Bi^{3+} ions residing in $(Lu,Gd)2O_8$, $(Lu,Gd)1O_8$ and $(Lu,Gd)3O_7$ polyhedrons, respectively, in view of the gradually stronger crystal field of the three sites.

With further doping of Gd^{3+} at *x* = 0.75 and *x*= 0.99, Bi^{3+} showed a completely

different broadband red emission ranging from 425 to 800 nm (centered at 610 nm). It is encouraging to find that the FWHM of this band is as high as 0.72 eV for the x = 0.75 sample and 0.70 eV for the x = 0.99 sample and the spectra cover the near-infrared (NIR) region. Such Bi^{3+} luminescence, though reported before,[8,13] is yet rather rare. The observed broadband red-NIR emission should be due to more distortion of the polyhedrons accommodating Bi^{3+} ions by the change of crystal structure and an enhanced nephalauxetic effect by a higher covalency of the Bi-O bond, as explained below.

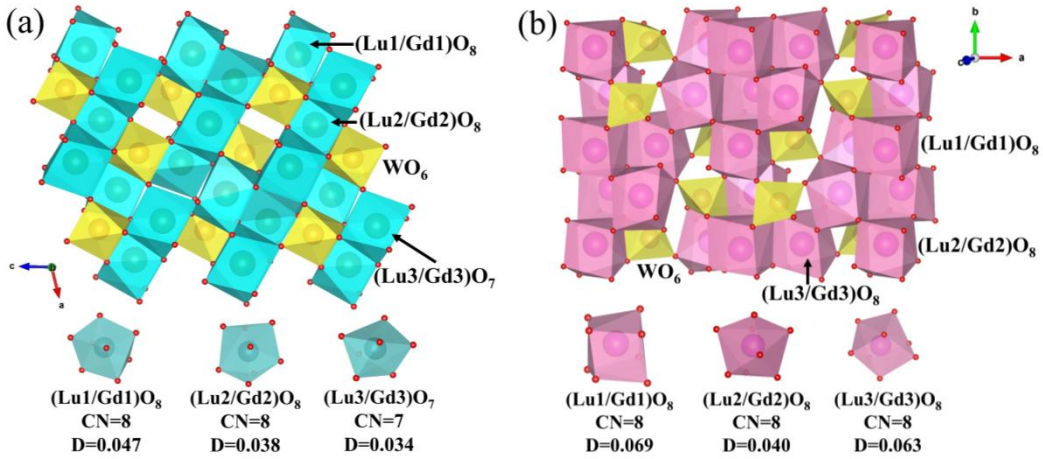

Fig. 7 The crystal structures of $(Lu_{0.99-x}Gd_xBi_{0.01})_2WO_6$ for x = 0-0.25 (a) and x = 0.75-0.99 (b).

As shown in Fig. 7, the crystal structure and type of polyhedron change with increasing Gd^{3+} doping. The polyhedrons where Bi^{3+} ions are accommodated change from [(Lu1/Gd1)O_8], [(Lu2/Gd2)O_8] and [(Lu3/Gd3)O_7] in the x = 0-0.25 samples to [(Lu1/Gd1)O_8], [(Lu2/Gd2)O_8] and [(Lu3/Gd3)O_8] in the x = 0.75-0.99 ones. With the broadband green emitting sample (x = 0.05) and broadband red emitting sample (x = 0.99) for example, polyhedral distortion index (D) was calculated with the following equation to quantitatively characterize the distortion of different polyhedrons:[41,42]

$$D=\frac{1}{n}\sum\frac{|l_i-l_{av}|}{l_{av}} \qquad (2)$$

Where l_i is the distance from the central atom to the i^{th} coordinating oxygen atom and l_{av} is the average bond length of (Lu/Gd/Bi)-O. As the D values for the x = 0.05 sample is lower than those of the x = 0.99 sample (Fig. 7), it can be said that the substantially higher polyhedral distortion of the x = 0.99 sample may have enhanced crystal splitting to lower the $^3P_1$ level of Bi^{3+} for the red-NIR luminescence. On the other hand, the electronegativity of Gd (1.20 eV) is smaller than that of Lu (1.27 eV). Therefore, significant substitution of Lu with Gd may lead to a stronger polarizability and covalency of the Bi-O bond if we consider (Lu/Gd)-O-Bi moiety. The stronger crystal field arising from an more significant nephelauxetic effect may also red-shift the luminescence of Bi^{3+}, as observed and proved by other researchers.[43-45] It may also be inferred from the blue-shifted emission of the $x \leqq 0.50$ samples that stronger bond covalency should may have played a more significant role in the luminescence behavior of the x = 0.75 and 0.99 samples. The sudden change of broadband green into broadband red-NIR emission without transition at x = 0.75, where crystal structure changes, indicates the importance of host lattice in Bi^{3+} luminescence. Moreover, the Gd^{3+} has special electronic configuration ($4f^7$) and may have effects on luminescence centers and cause the red-NIR emission. Gaussian fitting of the broad red-NIR band into three sub-bands did not yield convergent results, since the right-hand tail of the band extends to longer wavelengths and is out of the measured range of this work.

The PLE spectra of the x = 0-0.50 and x = 0.75-0.99 samples showed asymmetric bands centered at 346 and 333 nm, respectively (Fig. 6b). The excitation/emission wavelengths and the FWHM values are summarized in Table S5 for the series of $(Lu_{0.99-x}Gd_xBi_{0.01})_2WO_6$ phosphors. The quantum yield (QY) of the series samples was

also investigated and the results are shown in Table S5 and Fig. S6. It is seen that the QY value follows the variation trend of emission intensity and reached its maximum at x =0.05 (QY = 18.88%). The broadband red emission sample (x=0.99) has a QY value of 4.09%.

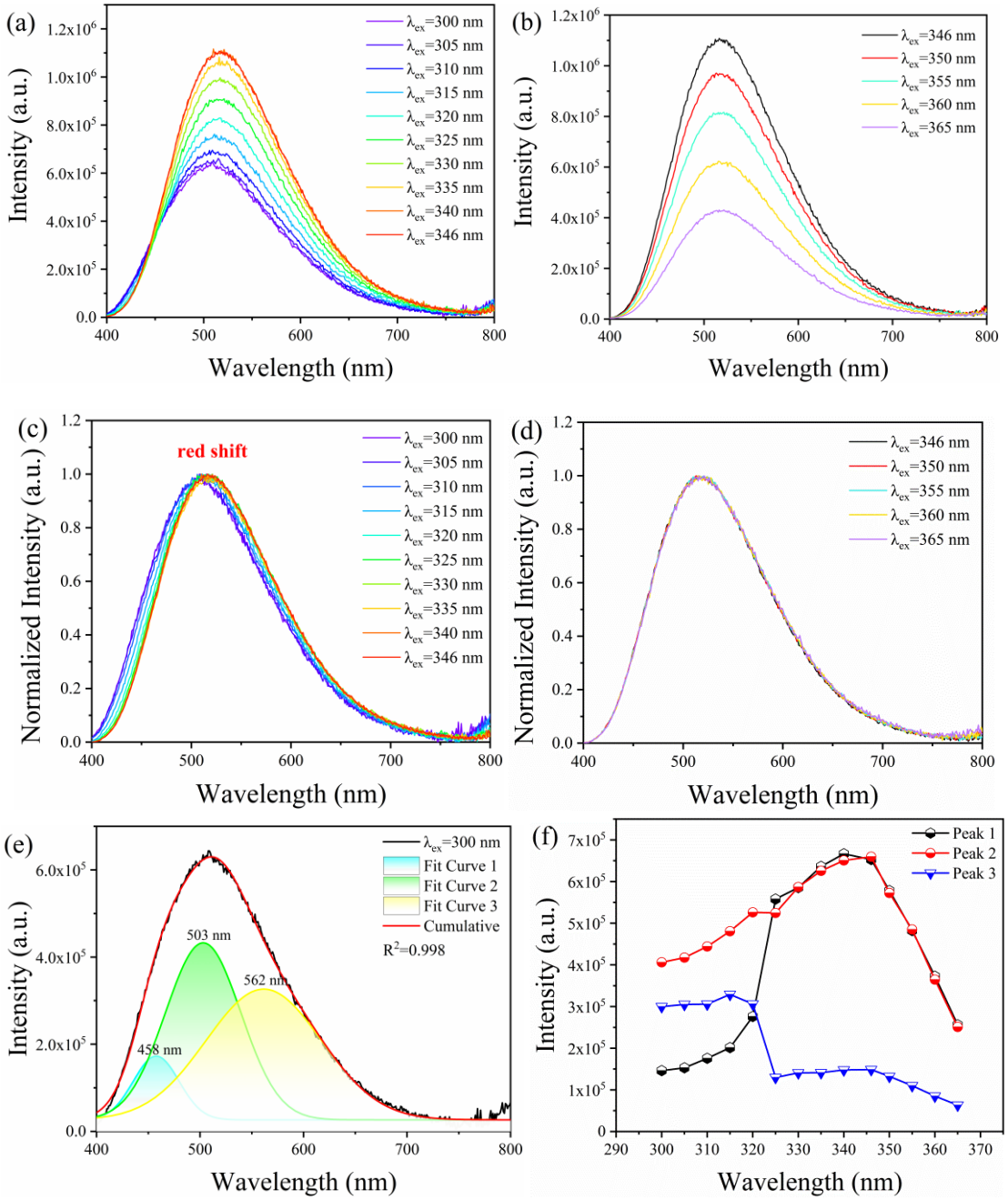

Fig. 8 The emission spectra (a, b) and intensity-normalized emission spectra (c, d) obtained under varying excitation wavelength in the range of 300-365 nm, Gaussian deconvolution of the emission band obtained under 300 nm excitation (e), and intensity variation of the deconvoluted three sub-bands with excitation wavelength (f) for the $(Lu_{0.94}Gd_{0.05}Bi_{0.01})_2WO_6$ phosphor.

As structure analysis revealed the existence of three different types of emission centers, each center should have its own excitation peak. This can be the reason for the asymmetric excitation bands in Fig. 6b. To further elucidate the luminescence behavior of Bi^{3+}, PL spectra were measured for the $(Lu_{0.94}Gd_{0.05}Bi_{0.01})_2WO_6$ phosphor by varying the excitation wavelength from 300 to 365 nm. As shown in Fig. 8a and Fig. 8b, the overall emission band did not show obvious profile change, but the intensity of emission varied and the strongest emission was obtained under 346 nm excitation, in accordance with the results of Fig. 6b. From the intensity-normalized PL spectra (Fig. 8c,d), it is seen that the center of the luminescence band tends to red-shift with increasing excitation wavelength until 346 nm. Gaussian deconvolution further revealed the variation trend of the three sub-bands for peak intensity and peak position, as shown in Fig. 8e, Fig. S7 and Table S6. Clearly, the intensities of sub-peaks 1 and 2 gradually increase till λ_{ex} = 346 nm and then decrease, showing an optimal excitation wavelength of 346 nm, while that of sub-peak 3 is basically unchanged till λ_{ex} = 315 nm and then substantially decreased at λ_{ex} = 325 nm, revealing that a short wavelength is more efficient for excitation. That is, site-selective excitation behaviors were observed for the multiple cation sites in the host.[5,16,45] Besides, the three sub-peaks were obviously red-shifted with increasing excitation wavelength from 300 to 335 nm (Table S6). For even longer excitation wavelength, sub-peaks 1 and 2 show basically unchanged position till λ_{ex} = 365 nm while sub-peak 3 keeps unchanged up to λ_{ex} = 355 nm and then obviously red-shifted. These largely corresponds with the observed peak-center variation for the overall

band with increasing excitation wavelength (Fig. 8c and d). Temperature-dependent emission spectra were also measured for the $(Lu_{0.94}Gd_{0.05}Bi_{0.01})_2WO_6$ sample. As exhibited in Fig. S8, the PL spectrum and peak position did not change with increasing temperature. The intensity of emission, however, decreased by 77.5% from 298 to 373 K, indicating that the thermal stability of luminescence needs improvement. The activation energy (ΔE) of thermal quenching can be calculated by using the Arrhenius equation, and a ΔE value of ~0.323 eV was obtained.

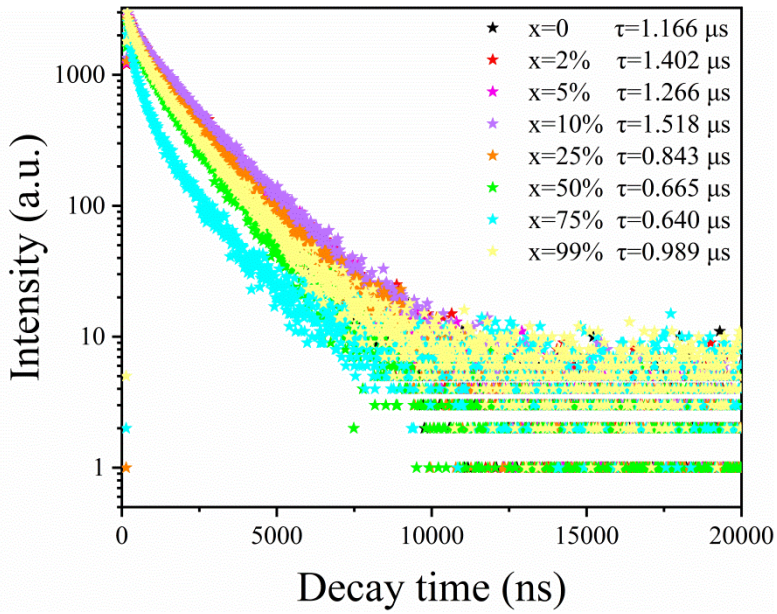

Fig. 9 Fluorescence decay curves for the main emissions of $(Lu_{0.99-x}Gd_xBi_{0.01})_2WO_6$ (x = 0-0.99), where λ_{ex} = 346 nm and λ_{em} = 510 nm for the x = 0-0.50 samples and λ_{ex} = 333 nm and λ_{em} = 610 nm for the x = 0.75-0.99 samples.

Fig. 9 shows the fluorescence decay curves for the main emissions of $(Lu_{0.99-x}Gd_xBi_{0.01})_2WO_6$ (x = 0-0.99) under the excitation of optimal wavelength. The curves can be fitted with the exponential polynomial $I(t)=A_1\exp(-t/\tau_1)+A_2\exp(-t/\tau_2)+A_3\exp(-t/\tau_3)$ (Fig. S9), where I(t) and t are the fluorescence intensity and decay time, respectively, A_1, A_2 and A_3 are constants, and τ_1, τ_2 and τ_3 are the decay time of exponential components. This corresponds well

with the presence of three types of luminescence centers. The average lifetime can be obtained using the equation of $\tau^* = \frac{A_1\tau_1^2+A_2\tau_2^2+A_3\tau_3^2}{A_1\tau_1+A_2\tau_2+A_3\tau_3}$. The fitting results, including the derived τ^*, $A_1/A_2/A_3$ values and the chi-square factor (χ^2) of fitting, are summarized in Table S7. The χ^2 values are around 1 for all the fittings, indicating the high quality of the fitting. It can be found that the average lifetime is in the ranges of 0.843-1.518 μs and 0.640-0.989 μs for the *x* =0-0.25 and *x* = 0.75-0.99 samples, respectively, and the *x* = 0.50 mixture sample has a lifetime of 0.665 μs.

3.3 Application of the broadband green phosphor in high color rendering white lighting

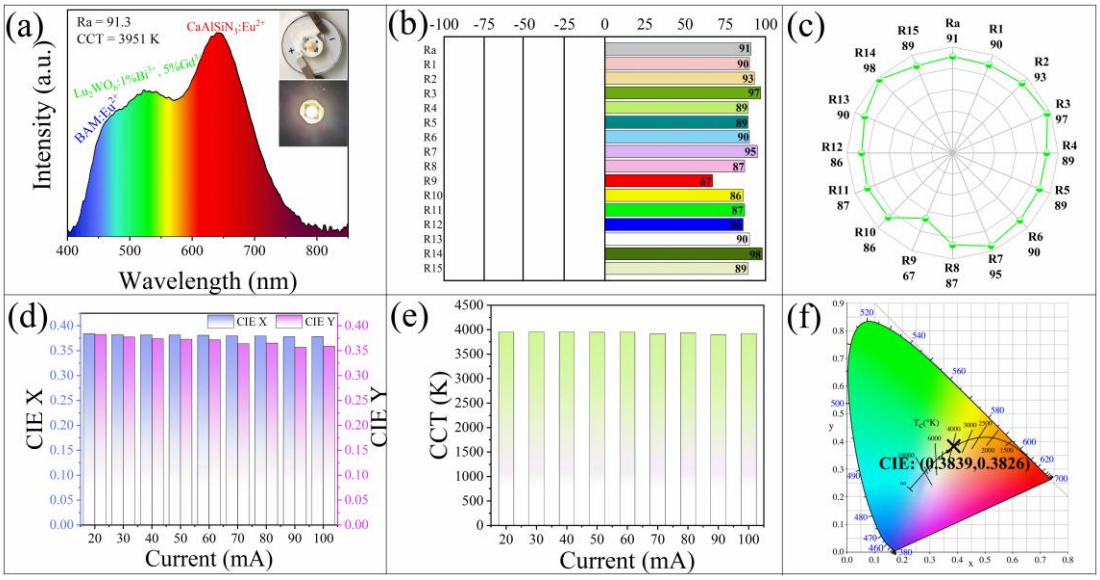

Fig. 10 The luminescence spectrum (a), color rendering index Ra and R1-R15 factors (b, c) and CIE chromaticity coordinates (f) of LED1 under 20 mA current driving. Parts (d) and (e) are for CIE and CCT under varying current of driving, and the inserts (a) show the appearances of the device with current on and off.

To evaluate the application potential of the $(Lu_{0.94}Gd_{0.05}Bi_{0.01})_2WO_6$ broadband green phosphor, a WLED device (LED1) was constructed using the R-G-B phosphor excited by UV-LED chip method, where the red and blue phosphors are commercially available $CaAlSiN_3:Eu^{2+}$ and BAM, respectively, and the excitation source is a 365 nm LED chip. Fig. 10a and Fig. 10f show the luminescence spectrum and the CIE

chromaticity coordinates of LED1 under 20 mA driving. It is seen that the device emits a warm white light and the luminescence spectrum covers the entire visible range, with the cyan gap being well covered. The device shows a satisfactory color correlated temperature (CCT) of 3951 K and a high Ra value of 91.3. In addition, all the other R parameters (R1-R15) are also satisfactory (Fig. 10b, c). To study the stability of the device, optical properties were measured by varying the driving current in the range of 20-100 mA, and the obtained main parameters are summarized in Table S8. It was found that CIE chromaticity coordinates remain almost stable at around (0.38, 0.38), indicating a high color stability of the device (Fig. 10d). Furthermore, the CCT of the device is quite stable at ~3900 K, irrespective of the driving current in the range of this study (Fig. 10e).

3.4 Application of the broadband red-NIR phosphor in simultaneous white and NIR lighting

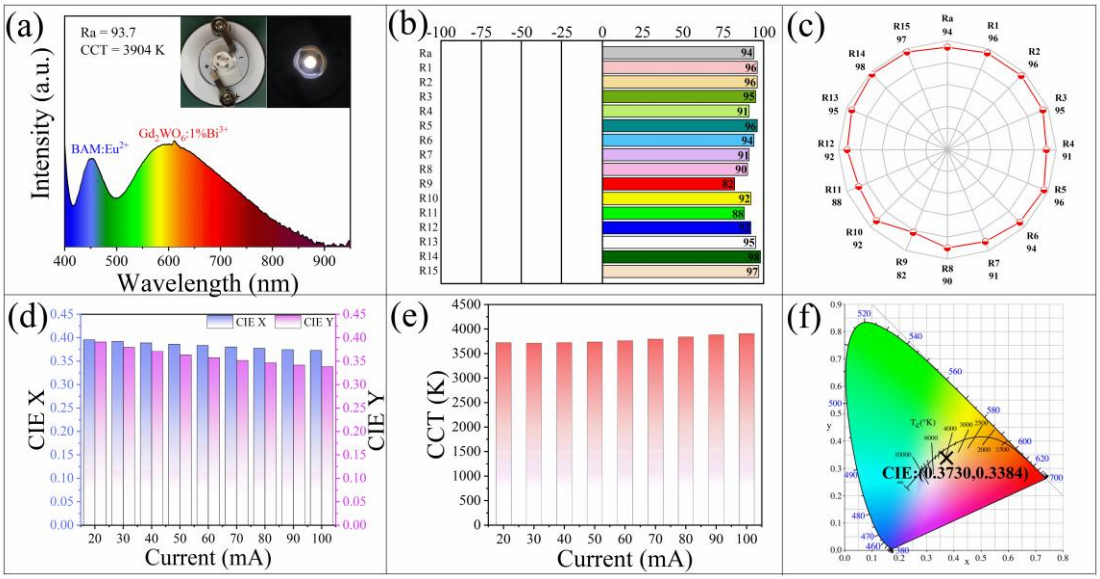

Fig. 11 The luminescence spectra (a), color rendering index Ra and R1-R15 factors (b, c) and CIE chromaticity coordinates (f) of LED2 under 100 mA current driving. Parts (d) and (e) are for CIE and CCT under varying current of driving, and the inserts (a) show the appearances of the device with current on and off.

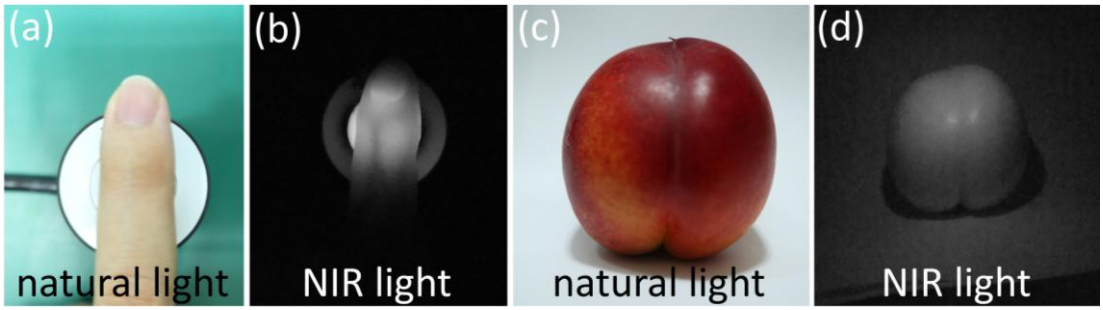

Fig. 12 Photographs of a finger (a, b) and a fruit (c, d) obtained under natural light (a, c) and the NIR light from LED2 (b, d).

The luminescence spectrum of $(Gd_{0.99}Bi_{0.01})_2WO_6$ has a large FWHM and covers a broad region from red to NIR, and thus the phosphor is promising for application in simultaneous white and NIR lighting. Fig. 11a shows the luminescence spectrum of LED2, which was fabricated using $(Gd_{0.99}Bi_{0.01})_2WO_6$, $BaMgAl_{10}O_{17}:Eu^{2+}$ green phosphor and a 365 nm LED chip. It is seen that the spectrum covers the entire visible range and the NIR region up to 900 nm. The device emits high-quality warm white light (inset of Fig. 11a), which has a relatively low CCT of 3904 K and a high Ra value of 93.7 (Fig. 11b). In addition, all the other R parameters (R1-R15) have satisfactory values (Fig. 11b, c). The optical properties of LED2 under different driving currents (20-100 mA) were measured, and the obtained main parameters are summarized in Table S9. It was found that the CIE chromaticity coordinates of the device slightly drifted from (0.39, 0.39) to (0.37, 0.34) with increasing driving current (Fig. 11d) and, accordingly, CCT slightly increased from 3721 K to 3904 K (Fig. 11e). As the luminescence spectrum of LED2 also covers the NIR region, application of the device in NIR imaging was also explored. Fig. 12 shows the photographs of a finger and a fruit taken under natural light and the NIR light from LED2. It can be seen from Fig. 12a,b that the finger can be noninvasively imaged and recognized, indicating potential application of the device in medical diagnosis. The photograph of the peach

can also be clearly captured by a NIR camera (Fig. 12 c and d), implying that the phosphor may also be applicable in night-vision technology.

Conclusions

Photoluminescence regulation of Bi^{3+} in Lu_2WO_6 was achieved *via* Gd^{3+} doping, and the effect of Gd^{3+} on phase composition, crystal structure, crystallite morphology and optical properties were systematically discussed. Application of the obtained typical phosphors in high color rendering index lighting, night vision and noninvasive imaging were also demonstrated. The main conclusions are as follows:

(1) Gd^{3+} doping greatly enhanced the crystallinity of the phosphor. The crystal structure of $(Lu_{0.99-x}Gd_xBi_{0.01})_2WO_6$ (x = 0-0.25) remained as that of monoclinic Lu_2WO_6 ($P2/c$ space group) up to x = 0.25 and then changed into that of monoclinic Gd_2WO_6 ($C2/c$ space group) at the high doping levels of x = 0.75-0.99.

(2) The photoluminescence of Bi^{3+} was tuned from broadband green to broadband red-NIR light with increasing Gd^{3+} doping. Three different kinds of Bi^{3+} centers were proved *via* crystal structure analysis, spectral analysis and fluorescence decay analysis to be responsible for the observed broadband emissions. White-LED device, with high color rendering index (Ra = 91.3), stable emission color, and low correlated color temperature (3951 K) can be fabricated with the broadband $(Lu_{0.94}Gd_{0.05}Bi_{0.01})_2WO_6$ green phosphor.

(3) LED device that simultaneously emits high color rendering white light and near-infrared light can be obtained with the broadband $(Gd_{0.99}Bi_{0.01})_2WO_6$ red-NIR phosphor for night version and noninvasive imaging applications.

Author contributions

Xuejiao Wang: conceptualization, funding acquisition, writing – review & editing. Xiaowen Feng: investigation, data curation, writing – original draft. Maxim S. Molokeev: data curation, resources. Huiling Zheng: data curation, resources. Qiushi Wang: investigation, data curation. Chunyan Xu: data curation, resources. Ji-Guang Li: conceptualization, supervision, funding acquisition. All authors contributed to the general discussion.

Conflicts of interest

There are no conflicts to declare.

Acknowledgements

This work is supported in part by the Project of Education Department of Liaoning Province (Grant No. LQ2019014) and Natural Science Foundation of Liaoning Province (Grant No. 2020-MS-286). The authors wish to thank the facility's support of the 4B9A beamline of the Beijng Synchrotron Radiation Facility (BSRF) (Project No. 2021-BEPC-PT-005290). The authors would like to thank Siqi Liu from Shiyanjia Lab (www.shiyanjia.com) for the XPS analysis.

References

1. Y. Xiao, W. Xiao, D. Wu, L. Guan, M. Luo and L. Sun, *Adv. Funct. Mater.*, 2022, **32**, 2109618.
2. D. Liu, G. Li, P. Dang, Q. Zhang, Y. Wei, H. Lian, M. M. Shang, C. Lin and J. Lin, *Angew. Chem. Int. Ed.*, 2021, **60**, 14644-14649.
3. F. He, E. Song, Y. Zhou, H. Ming, Z. Chen, J. Wu, P. Shao, X. Yang, Z. G. Xia and Q. Zhang, *Adv. Funct. Mater.*, 2021, **31**, 2103743.
4. F. Zhao, H. Cai, Z. Song and Q. Liu, *Chem. Mater.*, 2021, **33**, 8360-8366.

5. S. Wu, Q. Liu, P. Xiong, W. Chen, Q. Dong, D. Chen, D. Wang, G. Zhang, Y. Chen and G. Li, *Adv. Opt. Mater.*, 2022, 2102842.
6. Y. Wei, H. Yang, Z. Gao, X. Yun, G. Xing, C. Zhou and G. Li, *Laser Photonics Rev.*, 2016, **15**, 2000048.
7. W. Bai, S. Shi, T. Lin, T. Zhou, T. Xuan and R. J. Xie, *Adv. Photonics Res.*, 2021, **2**, 2000158.
8. S. You, Y Zhuo, Q. Chen, J. Brgoch and R. J. Xie, *J. Mater. Chem. C.*,2020 **8**, 15626-15633.
9. Q. Sun, S. Wang, L. Sun, J. Liang, B. Devakumar and X. Huang, *Mater. Today Energy.*, 2020, **17**, 100448.
10. Q. Zhang, X. Wang and Y. Wang, *J. Alloys Compd.*, 2021, **886**, 161217.
11. J. Y. Ding, Y. Wei, W. Liu, Y. Li, Q. Wu and J. Zhou, *Chem. Eng. J.*, 2021, **403**, 126382.
12. Z. Xu, B. Devakumar, N. Ma, W. Li and X. Huang, *J. Lumin.*, 2022, **243**, 118640.
13. W. Zhang, Y. Li, S. Ye, J. Zhou, D. Wu, C. Shi, M. Chen, J. Ding and Q. Wu, *Dalton Trans.*, 2021, **50**, 10446-10454.
14. L. Cao, W. Li, B. Devakumar, N. Ma, X. Huang and A. F. Lee, *ACS Appl. Mater. Interfaces.*, 2022, **14**, 5643-5652.
15. J. Y. Ding, Q. Xu, J. He, W. Zhang, J. Zhou and Q. Wu, *Mater. Chem. Front.*, 2021, **5**, 7251-7258.
16. P. Dang, Q. Zhang, D. Liu, G. Li, H. Lian, M. Shang and J. Lin, *Chem. Eng. J.*, 2021, **420**, 127640.
17. A. Krasnikov, A. Suchocki, V. Tsiumra, L. Vasylechko, L. Wachnicki, S. Zazubovich and Y. Zhydachevskyy, *J. Lumin.*, 2021, **235**, 118065.
18. H. Li, R. Pang, Y. Luo, H. Wu, S. Zhang, L. Jiang, D. Li, C. Li and H. Zhang, *ACS Appl. Electron. Mater.*, 2019, **1**, 229-237.
19. L. Pang, R. Liu, G. Sun, W. Li, D. Jiang, L. Zhang, S. Li, C. Feng and J. Zhang, *Inorg. Chem.*, 2018, **57**, 12303-12311.
20. S. Wang, T. Wang, X. Yu, Z. Li, L. Guo, J. Chen, F. Zhao, W. Feng, X. Xu and J. Qiu, *Inorg. Chem.*, 2021, **60**, 14467-14474.
21. D. Wang, Z. Tang, W. Khan and Y. Wang, *Chem. Eng. J.*, 2017, **313**, 1082-1087.
22. H. Yang, P. Li, X. Fu, Z. Ye, X. Huo, Y. Wang, Q. Wu, H. Suo, L. Li and Z. Wang, *Mater. Today Chem.*, 2022, **26**, 101050.

23. Bruker AXS TOPAS V4: General profile and structure analysis software for powder diffraction data. - User's manual, Bruker AXS, Karlsruhe, Germany 2008.
24. H. Zheng, R. Zhang, H. Han, C. Liu and Y. Yan, *J. Magn. Magn. Mater.*, 2019, **484**, 172-178.
25. Z. Zhang, H. Zhang, C. Duan, J. Yuan, X. Wang, D. Xiong, H. Chen and J. Zhao, *J. Alloys Compd.*, 2008, **466**, 258-263.
26. A. V. Tyulin and V. A. Efremov, *Kristallografiya*, 1987, **32**, 371-377.
27. Y. Wang, H. Xu, C. Shao and J. Cao, *Appl. Surf. Sci.*, 2017, **392**, 649-657.
28. C. D. Wagner, W. M. Riggs, L. E. Davis and J. F. Moulder, *Perkin-Elmer Corporation.*, 1992, **40**, 221.
29. Y. Shiraishi, I. Nakai, T. Tsubata, T. Himeda and F. Nishikawa, *J. Solid State Chem.*, 1997, **133**, 587-590.
30. S. Torrengo, M. C. Paul, A. Halder, S. Das, A. Dhar, J. K. Sahu, S. Jain, A. V. Kir'yanov and F. d'Acapito, *J Non Cryst Solids.*, 2015, **410**, 82-87.
31. H. Arfin, J. Kaur, T. Sheikh and S. Chakraborty, *Angew. Chen. Int. Ed.*, 2020, **59**, 11307-11311.
32. G. Blasse, *J. Solid State Chem.*, 1972, **4**, 52-54.
33. P. Boutinaud, *J. Lumin.*, 2020, **223**, 117219.
34. J. Xue, H. Li, H. M. Noh, B. C. Choi, S. H. Park, J. H. Jeong and J. H. Kim, *J. Lumin.*, 2018, **202**, 97-106.
35. X. Chen, Z. Zhang, A. Feng, M. Xu, J. Zhao and F. Xu, *Mater. Res. Bull.*, 2015, **70**, 26-31.
36. J. S. Bae, J. H. Jeong, S. Yi and J. C. Park, *Appl. Phys. Lett.*, 2003, **82**, 3629-3631.
37. J. S. Bae, J. H. Jeong, K. S. Shim, B. K. Moon, S. S. Yi, J. H. Kim, Y. S. Kim and J. S. Lee, *Appl. Surf. Sci.*, 2006, **252**, 4564-4568.
38. J. Jiang, H. Ren, F. Huang, L. Wang and J. Zhang, *CrystEngComm*, 2021, **23**, 6117-6127.
39. X. J. Wang, X. W. Feng, C. S. Gong, M. Sun, C. Wang, Q. S. Wang and J.-G. Li, *Adv. Powder Technol.* 2022, **33**, 103392.
40. P. Dang, D. Liu, X. Yun, G. Li, D. Huang, H. Lian, M. Shang and J. Lin, *J. Mater. Chem. C.*, 2020, **8**, 1598-1607.

41. K. A. Denault, J. Brgoch, M. W. Gaultois, A. Mikhailovsky, R. Petry, H. Winkler, S. P. DenBaars and R. Seshadri, *Chem. Mater.*, 2014, **26**, 2275-2282.
42. W. H. Baur, *Acta. Crystallogr. B. Struct. Sci. Cryst. Eng. Mater.*, 1974, **30**, 1195-1215.
43. F. Kang, H. Zhang, L. Wondraczek, X. Yang, Y. Zhang, D. Lei and M. Peng, *Chem. Mater.*, 2016, **28**, 2692-2703.
44. X. Wang, J. Wang, X. Li, H. Luo and M. Peng, *J. Mater. Chem. C.*, 2019, **7**, 11227-11233.
45. F. Kang, M. Peng, X. Yang, G. Dong, G. Nie, W. Liang, S. Xu and J. Qiu, *J. Mater. Chem. C.*, 2014, **2**, 6068.
46. P. P. Dang, S. S. Liang, G. G. Li, H. Z. Lian, M. M. Shang and J. Lin, *J. Mater. Chem. C*, 2018, **6**, 9990-9999.